

# Realistic behavior of infilled steel frames in seismic events: experimental and analytical study

Kaveh Faraji Najarkolaie<sup>1</sup> · Majid Mohammadi<sup>2</sup> ·  
Nader Fanaie<sup>1</sup>

Received: 17 September 2016 / Accepted: 12 June 2017  
© Springer Science+Business Media B.V. 2017

**Abstract** An experimental and analytical study is carried out to investigate the effects of lateral loading type on the behavior of masonry infilled steel frames. During earthquake the lateral load is applied as distributed loading to the top beams and columns through rigid floors; however, in most available experimental studies the lateral loading is applied as concentrated loading. In this study, two identical specimens are tested and their behavior is compared under distributed and concentrated lateral loadings. Finite element models of the specimens are also developed and validated against the experimental results. To have a better view, the influence of loading type is studied on another experimental specimen having concentrated loading. A parametric study is also conducted on the influence of loading type in multi-span frames and infills with different aspect ratios. The obtained experimental results show that the distributed loading results in 18.5 and 29% increase in the strength and stiffness of Infilled frames, compared to the case with concentrated loading. Less strength and stiffness in specimens subjected to concentrated loading is a result of stress concentration at the infill corner near the loading point which leads to premature corner crushing. Therefore, it is believed that the codes' formulas, mostly based on specimens with concentrated loading, are conservative, underestimating the real ultimate strength and stiffness of masonry infilled steel frames.

**Keywords** Masonry infill · Steel frame · Seismic load · Distributed lateral loading · In-plane behavior

---

✉ Majid Mohammadi  
M.Mohammadi@IIEES.ac.ir

Kaveh Faraji Najarkolaie  
kfaraji@mail.kntu.ac.ir

Nader Fanaie  
fanaie@kntu.ac.ir

<sup>1</sup> Department of Civil Engineering, K. N. Toosi University of Technology, Tehran, Iran

<sup>2</sup> International Institute of Earthquake Engineering and Seismology, Tehran, Iran

**List of symbols**

$H_{ult}$	Corner crushing strength
$K_{ult}$	Empirical constant for calculating infill strength
$t$	Net thickness of the infill
$I_{xx}$	Second moment of area of steel section
$A$	Section area
$f'_c$	Compressive strength of masonry prism
$\epsilon'_c$	Strain corresponding to the peak stress of the masonry prism
$\epsilon$	Flow potential eccentricity
$f_{b0}$	Initial equibiaxial compressive yield stress
$f_{c0}$	Initial uniaxial compressive yield stress
$K_c$	Second stress invariant ratio
$\mu_v$	Viscosity parameter
$\psi$	Dilation angle
$d_t$	Damage parameter for tension
$d_c$	Damage parameter for compression
$E$	Young's modulus
$b_c$	Empirical scalar parameters for compression damage
$b_t$	Empirical scalar parameters for tension damage
$w_t$	Tension stiffness recovery
$w_c$	Compression stiffness recovery
$\rho$	Density
$\nu$	Poisson's ratio
$f'_t$	Tensile strength
$\mu$	Friction coefficient
$f_b$	Compression strength of brick
$E_c$	Masonry prism Young's modulus
$t_n^0$	Peak tensile bond strength
$t_s^0$	Peak shear bond strength
$G_{IC}$	Mode I-fracture energy
$G_{IIC}$	Mode II-fracture energy
$G_C$	Mixed mode fracture energy
$E_m$	Mortar Young's modulus
$E_b$	Brick Young's modulus
$f_m$	Compressive strength of mortar
$h_m$	Mortar height
$K_n$	Normal stiffness
$K_s$	Shear stiffness
$G_b$	Shear modulus of brick
$G_m$	Shear modulus of mortar
$\delta_m^f$	Effective separation at complete failure
$\delta_m^0$	Effective separation at damage initiation
$\delta_m^{max}$	Maximum value of effective separation
$M$	Diagonal lumped mass matrix
$F$	Applied load vector
$I$	Internal force load vector
$\xi$	Fraction of critical damping of highest mode
$\omega_{max}$	Highest eigenvalue in the system

## 1 Introduction

Masonry infills are regularly applied in most structural systems in high seismic risk regions throughout the world. Unreinforced masonry (URM) panels, often employed for architectural purposes in both reinforced concrete and steel frames, are usually considered as non-structural elements. Thus their effect is either not included or simplified in the current design practices due to the design complexities. Ignoring URM associated role in the mechanical properties of the infilled frame such as strength, stiffness and ductility is not always safe and leads to inaccuracy of the analyses. During a seismic event, they interact with the bounding frames and attract lateral loads which may provide various failure mechanisms.

Over the last six decades, numerous extensive experimental and analytical researches have been conducted on structural effects of infill panels including studies which intend to investigate the effect of these panels on the behavior of infilled frames under lateral seismic loads (Mainstone and Weeks 1972; Mehrabi et al. 1996). There are different types of panels which are frequently used in steel structures as a partition such as sandwich panels, masonry, drywalls and etc. (De Matteis and Landolfo 1999; Liu and Soon 2012; Mohebbi et al. 2016). Several experimental studies have been carried out to investigate the effects of different partitions on the behavior of steel frames (Dawe and Seah 1989; De Matteis 2005). In this respect, the researchers have attempted to provide design approaches and procedures that consider the effect of these panels in buildings (Asteris et al. 2013; De Matteis and Landolfo 2000; El-Dakhkhni et al. 2003). It was concluded that panels have significant influences on the behavior of steel frames that should not be ignored in order to have a realistic design.

This study focuses on steel frames that use masonry panels as infill. Most of the seismic rehabilitation codes recommend replacing the masonry infill with single or multiple struts in order to consider the effects of these panels on the behavior both concrete and steel frames. Polliakov (1963) was the first who suggested “diagonal strut concept” method, which included replacing the infill with an equivalent diagonal strut. This method was further developed by Holmes (1961) and other researchers (Chrysostomou et al. 2002; Crisafulli and Carr 2007; Madan et al. 1997).

The analytical models, developed by researchers, are categorized in two groups of macro and micro models for simulating overall and detailed behaviors of the infilled frames, respectively (Chrysostomou et al. 2002). Various macro modeling studies were performed by many researchers. These studies, which are mostly based on the equivalent strut method, investigated the behavior of an infilled frame under monotonic loading (Barua and Mallick 1977; Smith and Carter 1969). Other methods such as multiple strut models and two diagonal struts were also developed to consider the presence of connectors and openings (Choudhury et al. 2015; Klingner and Bertero 1976; Liauw and Lee 1977; Mochizuki 1988; Thiruvengadam 1985). Crisafulli and Carr (2007) proposed a multi strut model which employed a 4 node element. In this model the compression and shear behavior of the masonry panel were represented with two struts and a shear spring respectively. Moreover, several micro modeling studies were developed to assess the behavior of an infilled frame in more specific details as well as different possible failure modes (Choudhury et al. 2015; Dhanasekhar and Page 1986; Kumar et al. 2014; Minaie et al. 2014).

According to previous studies infilled frames, subjected to lateral loading, are expected to show five different failure mechanisms: (1) diagonal cracking; (2) corner crushing; (3) sliding shear; (4) diagonal compression; and (5) frame failure (El-Dakhkhni et al. 2003).

Corner crushing is the most probable failure mode, anticipated in an infilled frame. Therefore, several approaches were developed by researchers to establish a method for determining corner crushing strength. These methods were mostly based on equivalent strut and plastic collapse theory (Liauw and Kwan 1983; Mainstone 1971; Saneinejad and Hobbs 1995; Smith and Coull 1991; Wood 1978). Masonry Standards Joint Committee (MSJC) (2008) has provided provisions for designing masonry infills, based on the studies conducted by Flanagan and Bennett (Flanagan and Bennett 2001; Caliò et al. 2012). They conducted several experimental tests on large scale steel frames infilled with clay tile and clay brick with various geometry and frame parameters to establish a simple formula as follows (Flanagan and Bennett 1999):

$$H_{ult} = K_{ult} t f'_c \quad (1)$$

in this formula  $H_{ult}$ ,  $K_{ult}$ ,  $t$ , and  $f'_c$  are corner crushing strength, empirical constant, net thickness of the infill and prism compressive strength of the masonry, respectively.

The proposed equations for determining infill strength are based on the failure modes obtained through the experimental tests and depends on the test setup arrangement (Liu and Manesh 2013). In almost all test setups of the experimental studies available in the literature, a concentrated load is applied to the specimen near the top beam to column connection (Fig. 1) (Dawe and Seah 1989; El-Dakhkhni et al. 2004; Ju et al. 2012; Moghaddam 2004; Mohammadi et al. 2010). However, in reality the applied seismic loads produce uniform displacements in the top beam regarding the rigid diaphragm of the roof. Therefore, to better simulate an earthquake phenomenon, it is more realistic to consider the lateral load as distributed in an experimental test. Figure 2 shows a common steel deck used in buildings. As it can be seen seismic load transfer to the infilled frame is different than that of usual test setups showed in Fig. 1.

This study investigates the effects of different types of lateral loading on the behavior of infilled steel frames. For this purpose, two identical specimens are subjected to distributed and concentrated lateral loading.

To further investigate the influence of different lateral loading types on behavior of a masonry infilled steel frame, finite element models of these specimens are developed and calibrated by experimental results. Later on, these simulations are used to perform a parametric study. The influence of number of spans and aspect ratio on the behavior of the infilled steel frame is investigated. In order to show that the obtained results do not depend on the test setup arrangement, another experimental study conducted by Moghadam et al.

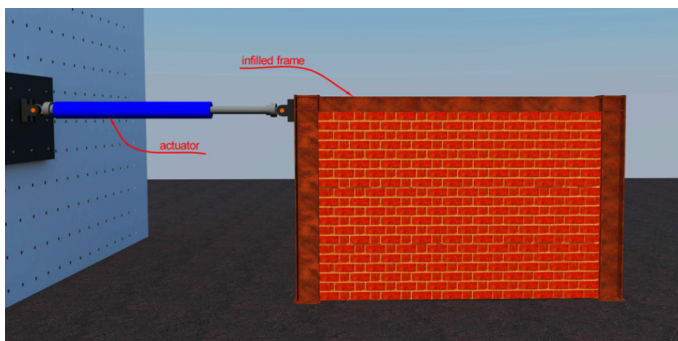


**Fig. 1** Regular test setup of infilled steel frames subjected to lateral loading

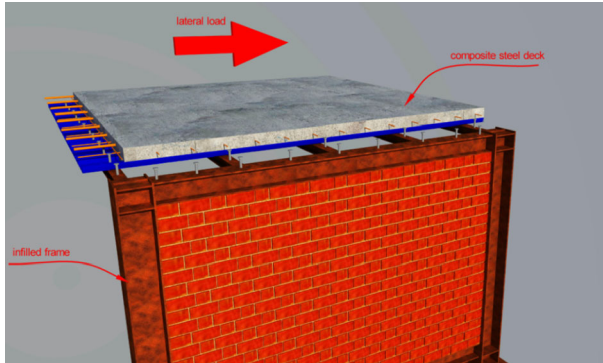


**Fig. 2** Realistic seismic load transferring for an infilled frame

(2006) is selected. This study includes a masonry infilled steel frame tested under concentrated lateral loading. The finite element model of the specimen is developed and its monotonic behavior is verified by the experimental data. After that, the model is subjected to distributed loading and its behavior is compared to that of specimen subjected with concentrated lateral loading.

## 2 Experimental study

### 2.1 Test setup and procedure

Test setups of the experiment are illustrated in Figs. 3 and 4. A four story building is designed in accordance with the uniform building code (UBC 1997). An infilled frame of the first story of the prototype is chosen to calculate the dimensions and sections of the test specimens. The main frame height, span length and wall thickness is 300, 450 and 20, respectively. The frame has column made of 2IPE 400 section and beam made of IPE 330 section. The provisions for scaling steel frames and masonry walls by Harris and Sabnis (1999) is employed in order to scale the infilled frame. The scaling ratio is selected with respect to frame height that could have been performed in the laboratory. The executable frame height is 150 cm which is half of the prototype frame height; therefore the

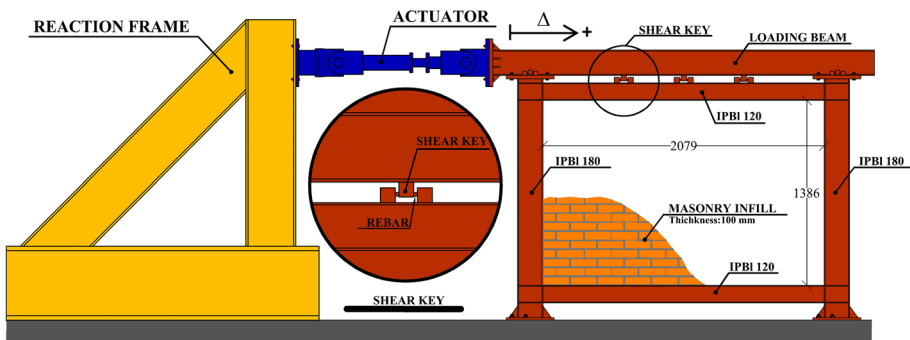


**Fig. 3** Schematic view of specimen DL (dimensions are in mm)

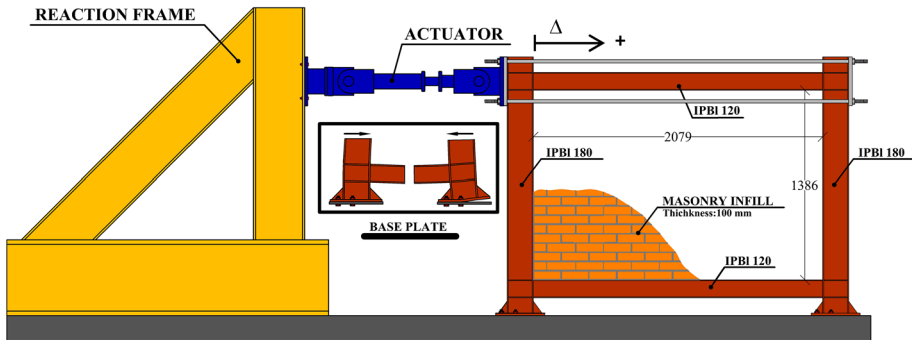


**Fig. 4** Schematic view of specimen CL (dimensions are in mm)

scaling ratio is considered as 1:2 of the actual structure dimensions. In this respect, the length of the test specimen is also reduced to 225 cm which is half of length of the prototype frame. Using the scale ratio, the sections area ( $A$ ) and moment of inertia ( $I_{xx}$ ) are multiplied by  $(\frac{1}{2})^2$  and  $(\frac{1}{2})^4$ . Available sections in the market with closest values to obtained  $A$  and  $I_{xx}$  are chosen for beam and columns of the test specimens.

Many studies are available in literature which has employed scaling method to study the behavior of masonry buildings or buildings with masonry infilled frame (Beyer et al. 2015; Krstevska et al. 2010; Lourenço et al. 2013; Tomažević and Weiss 2010). The purpose of these papers is usually studying the response of scaled buildings which are tested on the shake table. Nevertheless, this study aim to compare two scaled specimen and the differences in results that are obtained for scaled specimens should correlate with differences in results that would have been reached in full scale specimens. In this respect, the frame dimensions and sections are scaled based on the existing provisions. Therefore the only part that is left to be scaled is masonry wall. Since in current study, solid clay bricks have been used, the results of studies by Mohammed (2006) and Mohammed and Hughes (2011) which have the similar materials have been considered. The results of these studies showed that there was no considerable difference in strength and stiffness of the half scale specimen. However, changes were observed in friction and cohesion behavior between units of scaled specimen. In general, it was concluded that except for strength that is subjected to significant change in scaling ratios of 1:4 and 1:6, other parameters such as flexural strength, initial shear strength, bond strength and shear strength are not considerably influenced. It was mentioned that this remarkable change in strength in scaling ratios of 1:4 and 1:6 might be relevant to the production process of brick and the mortar thickness (Petry and Beyer 2014). So as an alternative Petry and Beyer (2014) stated to only change the brick thickness and keep the other dimensions of brick and mortar thickness the same. However, they mentioned this method results in less brick courses and probably lead to changing in strength and failure mode of the masonry wall. More recently a study has been conducted by Sathiparan et al. (2016) which investigate the effect of scaling on compression strength, shear strength, flexural strength of masonry cement block which its obtained results are opposed to the one by Mohammed and Hughes (2011). In this study compression strength has not been changed in different scaling, but shear and flexural strength are greatly varied.

Considering that there are different results and conclusions regarding scaling of masonry walls, in current study authors preferred to use bricks and mortars with original

dimensions. This approach reduces the brick courses and ultimately might slightly strengthen the masonry wall. Furthermore, the authors believe that the differences in dimensions are not that high to affect the failure mode. Also it should be noted that when masonry units are scaled, the influence of workmanship is increased and therefore another source of inaccuracy is involved in the experiment. Thus, in this study merely the wall thickness is halved and other dimensions of brick and mortar layer are considered similar to a full scale masonry wall.

Masonry units are solid clay brick with compression strength of 30 Mpa. The infill wall consists of  $196 \times 85 \times 65$  mm bricks and 10 mm thick mortar joints. The mortar mixture has 1:6 cement to sand ratio. The grade of steel used for this experiment is St37 steel. The column is constructed from standard IPB1 180 section with an area of  $45.3 \text{ cm}^2$  and second moment of area of  $2510 \text{ cm}^4$  about its major axis. The beam is constructed from standard IPB1 120 section with an area of  $25.3 \text{ cm}^2$  and second moment of area of  $606 \text{ cm}^4$  about its major axis. The flanges and web of beam are directly welded to the column flange. Two continuity plates are placed at each panel zone on the both sides of the frame. Table 1 shows the details of the test specimens.

The test setups of both specimens are exactly the same and their difference is in the loading method. Cyclic displacement control loading is applied to both specimens. Specimen DL is subjected to the distributed lateral loading applied through a loading beam of IPB1 220 section with 5 shear keys. Shear keys are in charge of transferring the horizontal loads to top of the beam. As shown in Fig. 3 a rebar is located at each side of the shear key and acts as roller so that the shear key does not prevent the beam from vertical movement. Specimen CL is subjected to the concentrated lateral loading, usually considered in regular experimental studies, shown in Fig. 4; the loading is applied as a concentrated force to the column, at the top beam to column connection.

The imposed cyclic lateral displacement history is based on FEMA461 (2006) shown in Fig. 5.

## 2.2 Material properties

Some tests were carried out in order to establish material properties of the steel frames and the infill walls. The frame material test was conducted on samples taken from the web of the beam members. The obtained values for modulus of elasticity and yielding stress were 199.9 GPa and 320 MPa respectively. To determine the material properties of masonry units, 10 masonry prism specimens were constructed which included 3 bricks and 2 mortar layers. The averages that are obtained for compressive strength and modulus of elasticity of these prism specimens are 9.5 and 1425 MPa, respectively. The prism specimens were cured under the same circumstances of the test specimens. The strain corresponding to the peak stress of the prism specimens ( $\epsilon'_c$ ) is equal to 0.01. Also based on the material tests, the mortar compressive strength is obtained as 7.5 MPa.

**Table 1** Details of the test specimens

Specimen ID	Loading type	Max lateral displacement (% drift)
DL	Distributed	7.4
CL	Concentrated	7.7

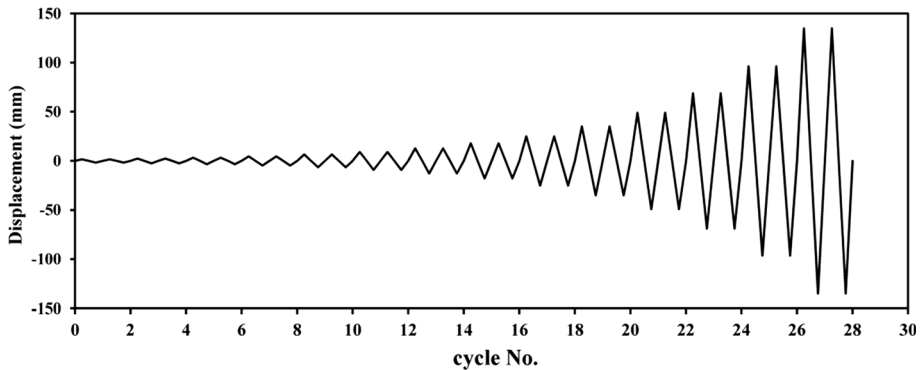


**Fig. 5** Displacement history

## 2.3 Experimental results

Lateral load-drift curves of the specimens DL and CL are illustrated in Fig. 6. Due to the support condition of the column base, lateral load in positive loading direction is greater than the opposite direction. As shown in Fig. 4 the bolts of base plate is so arranged to have rigid connection in positive direction and almost pinned connection in negative direction. Stiffness of the specimen DL is equal to 13.4 and 9.7 kN/mm in positive and negative loading direction respectively. As indicated in Fig. 6a the maximum recorded shear force in positive loading direction occurs at 5.1% drift and is 325 kN while it is 218 kN in negative loading direction, occurred at 3.5% drift. The stiffness of the specimen CL in positive and negative loading direction is 10.6 and 7.3 kN/mm, respectively. Also the maximum strength of the specimen in positive and negative loading direction is equal to 272.1 and 211.9 kN, respectively (Fig. 6b).

Figure 7 shows cracks and failure modes at the end of the test. In specimen DL sliding cracks were developed in the middle of the infill panel in early loading cycles. At 1.7% drift cracks inclined at approximately  $60^\circ$  against horizontal axis were initiated and propagated through the infill specimen which lead to formation of compression strut. This strut was initiated at bottom compression corner and continued to the top beam at approximately  $60^\circ$ . As it can be observed in Fig. 6a stiffness degradation is negligible in early drifts. However as the crack extends, the stiffness degradation increases. As it can be seen in Fig. 7a the predominant failure mode of this specimen is diagonal cracking and

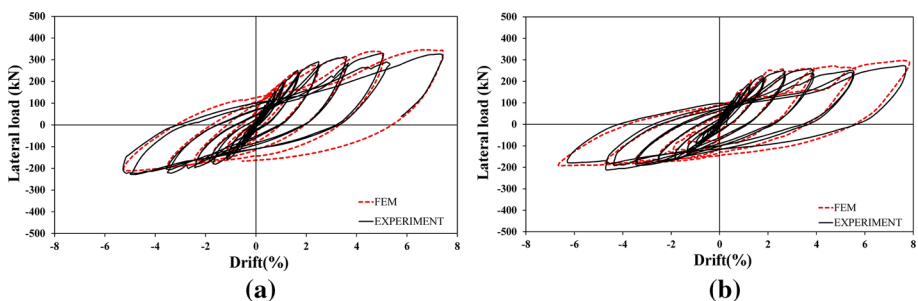


**Fig. 6** The experimental and analytical lateral load-drift curve **a** Specimen DL, **b** Specimen CL



**Fig. 7** Crack formation and failure modes at the end of the test **a** Specimen DL, **b** Specimen CL

although damage can be observed in the corners, corner crushing is not the dominant failure mode. Ultimately, due to the damage in the masonry panel, a minor strength loss is observed in negative loading direction of the lateral load-drift curve (Fig. 8) and therefore the test was terminated.

In specimen CL the first cracks were developed at 0.8% drift in the infilled panel. As loading continued, these cracks were gradually spread along two compression struts which were developed in each half cycle. Similar to specimen DL, with extension of cracks in the masonry panel, considerable stiffness degradation is observed in the lateral load-drift curve. At 5.5% drift, beam to column connection at left corner was damaged. Same thing occurred to the beam to column connection at right corner in the last negative cycle with 6.3% drift which has caused strength loss in negative loading direction and it is evident in Fig. 8. Consequently the test was terminated due to the failure of the surrounding frame. Figure 7b shows the specimen CL at the end of the test. As it can be seen, corner crushing is the dominant failure mode in this specimen which occurs in positive loading direction.

Cyclic load-drift envelope curve is utilized to compare the stiffness and strength of the specimens under distributed and concentrated loadings. A smooth “envelope” curve shall be drawn through each point of peak displacement during the first cycle of each increment of the loading according to ASCE/SEI 41-06 (2007). Figure 8 shows the envelope curves of the specimens. As it can be seen, there is a significant difference between the strength

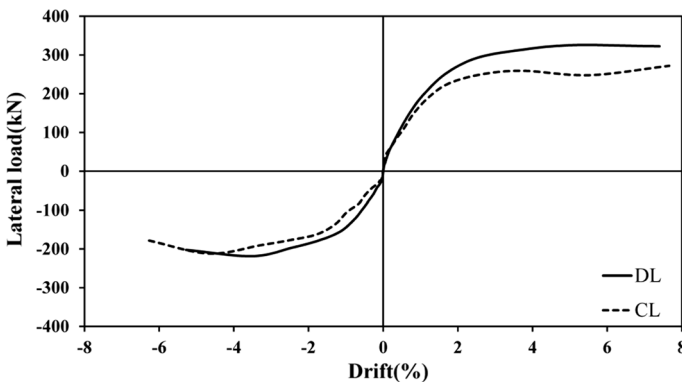


**Fig. 8** Envelope curves of specimens DL and CL

and stiffness of specimens. The strength of specimen DL is almost 18.5 and 3% higher than that of specimen CL in positive and negative loading direction, respectively. Also the stiffness of the DL is 26 and 33% greater than that of specimen CL in positive and negative loading direction, respectively. However, according to hysteresis curves in Fig. 6, both specimens have almost similar amount of strength degradation in repeated cycles.

### 3 Analytical study

Finite element analysis has been proved to be a powerful tool to meticulously examine the aspects that are difficult to study in an experimental study. A validated finite element model of an experimental work can be utilized in a comprehensive parametric study and therefore save time and diminish unnecessary expenses. In this regard, 3D finite element models of the experimental specimens are developed and their hysteresis behavior under distributed and concentrated lateral loading is verified by the experimental results. These models are employed to evaluate the influence of types of loading on the force distribution in masonry infilled steel frames. Finite element modeling is also used to investigate the behavior of an infilled specimen with different test setup under distributed and concentrated loading. Afterwards, a parametric study is performed on the finite element models of the experimental specimens.

Micro modeling method is used for analytical modeling of the current study. Non-linear analysis of the specimens is performed using ABAQUS (Hibbit et al. 2012). The following section describes the detailed procedure of finite element modeling:

#### 3.1 Development of finite element models

All elements are modeled using 3D deformable solid elements, available in ABAQUS program. The elements dimensions are in accordance with Sect. 2. The mortar joint as an independent masonry unit increases computational cost (Mohyeddin et al. 2013). Therefore, as discussed earlier, micro modeling method is employed for finite element modeling of the wall. Thus, instead of considering the wall as one integrated masonry unit, the bricks are modeled separately. Half of the mortar joint thickness is added to the adjacent brick layers.

##### 3.1.1 Material modeling

Concrete damage plasticity (CDP) approach is used to model inelastic behavior of the masonry. This modeling method is an appropriate choice for modeling isotropic brittle materials such as masonry units (Minaie et al. 2014; Moradabadi et al. 2015; Page 1981). Five parameters are required to define CDP, four of which have default values in ABAQUS: ( $\epsilon$ ), flow potential eccentricity, equal to 0.1 based on ABAQUS user manual;  $f_{b0}/f_{c0}$ , the ratio of Initial equibiaxial compressive yield stress to initial uniaxial compressive yield stress, equal to 1.16 according to both user guidelines and literature (Page 1981);  $K_c$ , second stress invariant ratio, equal to 0.667; and  $\mu_v$  is viscosity parameter. Implicit solver encounters convergence difficulty when elements experience softening behavior. In order to overcome this problem  $\mu_v$  is defined (Tiberti et al. 2016). However, since explicit procedure does not require convergence checking,  $\mu_v$  is considered as zero in this study.

**Table 2** Defining parameters of CDP model

Defining parameters	Dilation angle ( $\psi$ )	Eccentricity ( $\epsilon$ )	$f_{b0}/f_{c0}$	$k_c$	Viscosity parameter
Values	10	0.1	1.16	0.667	0

Different values have been suggested by researchers to define dilation angle ( $\psi$ ). CDP defining parameters are listed in Table 2.

Lourenco (1996) recommended the dilation angle of zero when mortar is subjected to confinement effect. Choudhury et al. (2015) used the value of 10° in his finite element analysis. Values of 20° and 30° were also assumed in other analytical studies (Agnihotri et al. 2013; Pereira et al. 2015). Since no particular value has been specified for dilation angle in the literature, in the present study different values are tested and the value of 10° is found to generate analytical results which are were consistent with the experimental ones.

CDP modeling implements the yield function proposed by Lubiner et al. (1989) to define strength properties under tension and compression. Figure 9 presents the yield surface corresponding to the yield function.

Cyclic loading results in degradation of stiffness. Damage parameter is required to meticulously model the behavior of masonry. Krätzig and Pölling (2004) suggested a formula to compute the damage parameter for tension ( $d_t$ ) and compression behavior ( $d_c$ ) material as follows:

$$d_{c/t} = 1 - \frac{f_{c/t} \cdot E^{-1}}{\epsilon_{c/t}^{pl} \left( \frac{1}{b_{c/t}} - 1 \right) + f_{c/t} \cdot E^{-1}}, \quad \epsilon_{c/t}^{pl} = b_{c/t} \cdot \epsilon_{c/t}^{in} \tag{2}$$

where,  $E$  is the initial elastic modulus;  $f_c$ ,  $\epsilon_c^{pl}$  and  $\epsilon_c^{in}$  are the current compressive stress, corresponding plastic strain and corresponding inelastic strain, respectively;  $f_t$ ,  $\epsilon_t^{pl}$  and  $\epsilon_t^{in}$  are the current tensile stress, corresponding plastic strain and corresponding inelastic strain, respectively;  $b_c$  and  $b_t$  are scalar parameters both with the values between zero and one. Their exact values are determined for concrete through experiment (Krätzig and Pölling 2004). Pölling (2000) suggested  $b_c = 0.7$  and  $b_t = 0.1$  for concrete. In this study, the same values were used in CDP modeling of masonry material in finite element analysis.

Cyclic loading might be associated with formation and closure of cracks or opening of them, which will lead to stiffness recovery upon changing of the direction of applied load. Since this is a significant mechanical characteristic of the quasi-brittle material such as masonry and concrete, ABAQUS has provided an option to specify the amount of stiffness recovery by the factors  $w_t$  and  $w_c$  tension stiffness recovery and compression stiffness recovery, respectively. It has been proven through experiments that during cyclic loading when load direction changes from tension to compression, compressive stiffness is recovered due to the closing of the cracks. However, when the applied load direction changes from compression to tension, tensile stiffness is not recovered since it leads to opening of the existing micro cracks (Fig. 10). ABAQUS considers this phenomenon as the default behavior of the aforementioned material by assigning the values of zero and one to  $w_t$  and  $w_c$  respectively (Hibbit et al. 2012).

Bolhassani et al. (2015) presented a method for simplified micro modeling of masonry walls with grouted and hollow units. The masonry units and mortar layers were modeled as a single homogenous material. Properties which were obtained in series of experimental

**Fig. 9** Yield surface in plane stress (Hibbit et al. 2012)

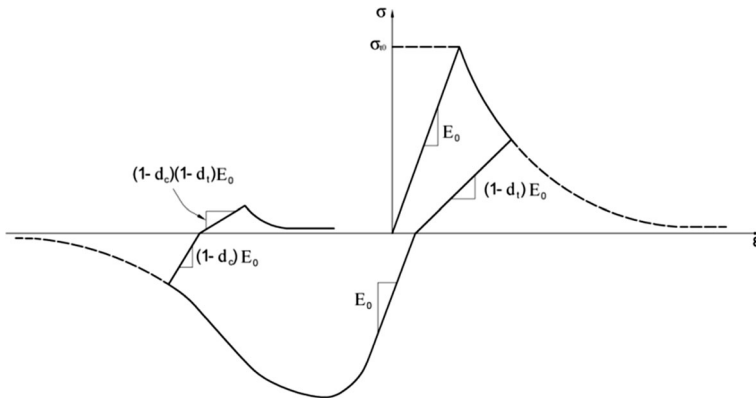
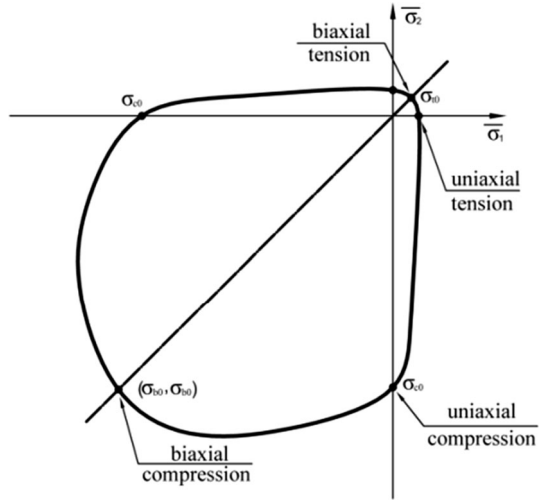
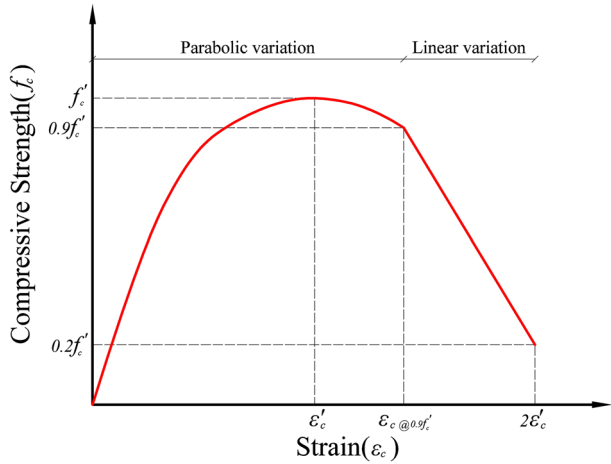


**Fig. 10** Stiffness recovery model (Hibbit et al. 2012)

tests were used to define the behavior of models. It was concluded that the analytical results are in good correlation with experimental ones. Agnihotri et al. (2013) studied the effect of in-plane damage on the out-plane behavior of masonry walls using non-linear finite element analysis. The model presented by Kaushik et al. (2007) for masonry prisms were used to simulate the compressive behavior of masonry. Based on the aforementioned papers the constitutive model, proposed by Kaushik et al. (2007), is employed to define compressive behavior of the masonry panel in this study. This model suggests that masonry stress–strain curve in compression (Fig. 11) can be considered as two parts, ascending parabolic part and descending linear part. The former can be represented in forms of stress and strain ratio as follows:

$$\frac{f_c}{f'_c} = 2 \frac{\epsilon_c}{\epsilon'_c} - \left( \frac{\epsilon_c}{\epsilon'_c} \right)^2 \tag{3}$$

**Fig. 11** Stress-strain curve of masonry units in compression



where,  $f_c$  is compressive stress in masonry;  $f'_c$  is peak stress;  $\epsilon_c$  is compressive strain; and  $\epsilon'_c$  is peak strain corresponding to peak stress. Using the recommendation by Angelillo et al. (2014) the tensile strength ( $f'_t$ ) of the brick is considered between 0.03 and 0.1 of its compression strength.

### 3.1.2 Interface modeling

While cohesive stiffness in the interface of bricks is undamaged, only the cohesive bond contributes to the shear forces and not the friction. However, when damage is considered, as the cohesive strength begins to degrade the friction activates, therefore a combination of both cohesive and friction contribute to the shear stresses. When tangential displacement between two surfaces reaches a point which results in full degradation of cohesive strength, only the friction contributes to the shear stresses (Hibbit et al. 2012). The friction coefficient varies from 0.7 to 1.2 which depends on the different mortar ratios (Pluijm 1999). While different values of friction coefficient have been used in studies, Angelillo et al. (2014) recommended to use the value of 0.75 when more detailed data is not available.

In this study bilinear curves as shown in Fig. 12 are employed for defining cohesive behavior of the interface. In a study by Bolhassani et al. (2015) bilinear curves were used for modeling the shear behavior and the analytical results were in good agreement with experimental results. Normal stiffness ( $K_n$ ) and shear stiffness ( $K_s$ ) should be determined in order to define the cohesive behavior. These parameters are calculated as follow (Lourenco 1996):

$$K_n = \frac{E_b E_m}{h_m (E_b - E_m)} \tag{4}$$

$$K_s = \frac{G_b G_m}{h_m (G_b - G_m)} \tag{5}$$

where  $E_b$  is brick Young’s modulus,  $E_m$  is mortar Young’s modulus,  $h_m$  is mortar height,  $G_b$  is Shear modulus of brick and  $G_m$  is shear modulus of mortar. The  $h_m$  is mentioned in Sect. 2.1. The  $E_b$  and  $E_m$  are considered in accordance with results of study by Kaushik

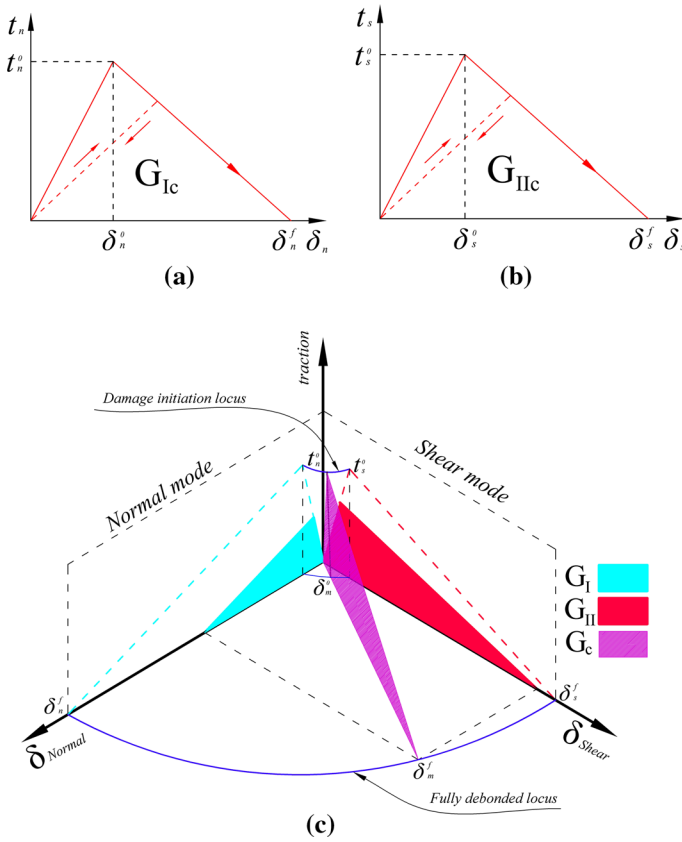


**Fig. 12** **a** Tensile behavior of interface, **b** Shear behavior of interface, **c** Combination of shear and tensile behavior of interface, (Camanho et al. 2003; Harper and Hallett 2008)

et al. (2007) and are equal to 300 times compressive strength of brick ( $f_b$ ) and 200 times compressive strength of mortar ( $f_m$ ), respectively and Poisson’s ratio is assumed to be 0.15.

The interface damage starts when the quadratic function as shown in left side of Eq. (6) equals one. In this equation  $t_n$  and  $t_s$  are normal and shear stress at bricks interface, respectively.  $t_n^0$  and  $t_s^0$  are peak tensile bond strength and peak shear bond strength (Nazir and Dhanasekar 2013). In a study by Lumantarna et al. (2012), It was determined that  $t_n^0$  and  $t_s^0$  are in direct relationship with compression strength of mortar. However these parameters are not related to strength of masonry prism. In the aforementioned study, the values of  $0.031 f_m$  and  $0.055 f_m$  were recommended for  $t_n^0$  and  $t_s^0$ , respectively. In current study same values are adopted for these parameters.

$$\left(\frac{t_n}{t_n^0}\right)^2 + \left(\frac{t_s}{t_s^0}\right)^2 = 1 \tag{6}$$

Power model is employed in current study to model decohesion under mixed mode loading. The  $\alpha$  is set equal to 2 based on recommendation by Tao (2013).

$$\left(\frac{G_I}{G_{IC}}\right)^\alpha + \left(\frac{G_{II}}{G_{IIC}}\right)^\alpha = 1 \tag{7}$$

In this equation,  $G_{IC}$  and  $G_{IIC}$  are mode I and II fracture energy.  $G_I$  and  $G_{II}$  are work which is a result of traction and its corresponding displacement in normal and shear directions respectively. Using the recommended values by Angelillo et al. (2014)  $G_{IC}$  is considered equal to 0.012 N/mm. The ductility index for shear fracture energy (ratio between fracture energy  $G_{IIC}$  and shear strength) is considered equal to 0.093 mm. Figure 12a, b and c illustrate the pure tensile, pure shear and combination of tensile and shear behavior of interface, respectively. In the Fig. 12c the  $G_C$  represents mixed mode fracture energy.

In this study linear softening is used for defining damage evolution, damage rate,  $D$ , is calculated as follows (Hibbit et al. 2012):

$$D = \frac{\delta_m^f (\delta_m^{max} - \delta_m^0)}{\delta_m^{max} (\delta_m^f - \delta_m^0)} \tag{8}$$

in which  $\delta_m^f$  is the effective separation at complete failure,  $\delta_m^0$  is effective separation at damage initiation and  $\delta_m^{max}$  maximum value of effective separation reached during loading history. Further explanation about calculating  $\delta_m^0$ ,  $\delta_m^f$  and  $G_C$  can be find in a study by Camanho et al. (Camanho et al. 2003; Harper and Hallett 2008).

### 3.1.3 Analysis method

Explicit dynamic procedure was employed for the analysis. Unlike implicit procedure, this non-linear analysis method determines the solution without iterations and convergence checking. This method is appropriate for solving the problems which include numerous contact elements and experience high discontinuities such as buckling and material degradation. As mentioned earlier, in the finite element analysis, masonry units have been modeled separately, which leads to creating a large number of cohesive elements that experience softening. Therefore, explicit dynamic was chosen as an analysis method, due to providing efficient and reasonable solutions to such problems as well as reducing computational costs (Dhanasekar and Haider 2008).

The explicit method employs Newton’s second law to calculate the acceleration at each moment (Eq. 9). The explicit central difference integration rule is employed to integrate the equation of motion as follows (Hibbit et al. 2012):

$$\ddot{u}^j = M^{-1} \cdot (F^j - I^j) \tag{9}$$

$$\dot{u}^{(j+\frac{1}{2})} = \dot{u}^{(j-\frac{1}{2})} + \frac{\Delta t^{(j+1)} + \Delta t^{(j)}}{2} \ddot{u}^{(j)} \tag{10}$$

$$u^{(j+1)} = u^{(j)} + \Delta t^{(j+1)} \dot{u}^{(j+\frac{1}{2})} \tag{11}$$

in which,  $\ddot{u}^j$  is the acceleration vector,  $M$  is diagonal lumped mass matrix,  $F$  is applied load vector,  $I$  is internal force load vector and  $\dot{u}$  is velocity vector. The superscript  $j$  represent increment number and in this respect  $(j - \frac{1}{2})$  and  $(j + \frac{1}{2})$  indicate mid increment values.

The explicit procedure uses  $\dot{u}^{(j-\frac{1}{2})}$  and  $\ddot{u}^j$  parameters, which are known, to obtain the unknown values of  $\dot{u}^{(j+\frac{1}{2})}$  and  $u^{(j+1)}$  using the Eqs. (10) and (11) respectively. The strain and stress at  $j + 1$  increment are calculated using the corresponding displacement at this point ( $u^{(j+1)}$ ) and therefore the internal force vector  $F^{j+1}$  can be computed. Since lumped mass  $M$  and applied load  $F$  are known values it is possible to calculate  $\ddot{u}^{j+1}$  using the Eq. (9), thus this procedure continues (Wu and Gu 2012). As it is obvious, to start the procedure and compute the  $u^1$ , the value of  $\dot{u}^{(-\frac{1}{2})}$  should be defined. Further details regarding this matter are presented elsewhere (Hibbit et al. 2012). This procedure is computationally efficient since it is easy to obtain the inverse of diagonal lumped mass matrix and it is not required to compute the stiffness matrix.

As it was mentioned earlier, the explicit procedure is computationally efficient in each increment; however, the procedure is conditionally stable. In order to provide stability, increments must be very small and meet the condition in Eq. (12); so that the procedure would remain stable (Hibbit et al. 2012).

$$\Delta t \leq \frac{2}{\omega_{max}} \left( \sqrt{1 + \zeta^2} - \zeta \right) \quad (12)$$

in which,  $\zeta$  is the fraction of critical damping associated with the highest mode and  $\omega_{max}$  is the highest eigenvalue in the system.

### 3.2 Specimens DL and CL

As mentioned earlier, in the experimental study, specimen CL was subjected to lateral loading at the top beam to column connection. However, in specimen DL lateral load was applied to the top beam with a loading beam through five shear keys. In specimen CL, it was applied to the same loading surface at the column as in the experiment. In specimen DL, the distributed loading was applied uniformly throughout the surface of beam top flange and the columns.

The infilled frame was discretized by tri-dimensioned continuum first-order elements with reduced integration (C3D8R available in ABAQUS library). A mesh study was conducted and mesh elements with the dimensions of  $50 \times 50$  mm was selected. All members in this analysis have the same element shape and size. Geometry and mesh details of the specimens are illustrated in Fig. 13. Necessary material properties that should be defined in modeling are listed in Table 3. The correlation study is presented in Sect. 3.2.1.

#### 3.2.1 Finite element modeling results

In Fig. 6 lateral load-drift curves of finite element models are compared to that of experimental ones. As it is demonstrated, finite element modeling can properly estimate the behavior of the specimens; up to 4% drift both curves are completely matched. However, after 4% drift, the strength of the finite element model is higher than that of the experimental test. This can be justified based on this fact that when the experimental specimen is subjected to cyclic loading, some cycles are repeated twice which lead to further degradation of the strength of infilled frame. However, in the finite element simulation each cycle is only applied once.

#### 3.2.2 Comparing the stress distribution in the specimens

This section presents compressive stresses of the infilled frame of both specimens at the drifts of 1, 3, 5 and 7%. As it is shown in Fig. 14, the second compression strut in the

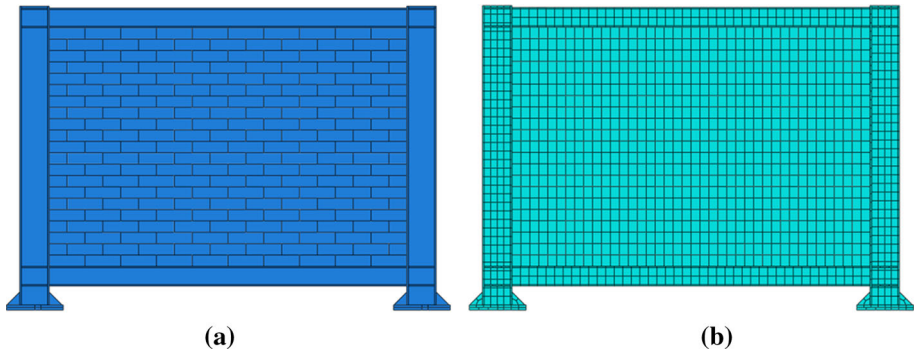


**Fig. 13** Geometry and mesh details of specimen DL and CL **a** Specimen geometry, **b** Mesh details of the specimen

**Table 3** Material properties of Infill panel used for verification of FE model

Property	Value
Density ( $\rho$ )	1812 kg/m <sup>3</sup>
Young's modulus ( $E$ )	1425 MPa
Poisson's ratio ( $\nu$ )	0.15
Compressive strength ( $f'_c$ )	9.5 MPa
Tensile strength ( $f'_t$ )	0.95 MPa
Strain corresponding to peak stress ( $\epsilon'_c$ )	0.01
Friction coefficient ( $\mu$ )	0.75
Compressive strength of mortar ( $f_m$ )	7.4 MPa
Peak tensile bond strength ( $t_n^0$ )	0.23 MPa
Peak shear bond strength ( $t_s^0$ )	0.4 MPa
Normal stiffness ( $K_n$ )	177 GPa
Shear stiffness ( $K_s$ )	77 GPa
Mode-I fracture energy ( $G_{IC}$ )	0.012 N/mm
Mode-II fracture energy ( $G_{IIC}$ )	0.037 N/mm

specimen DL is formed earlier than that in specimen CL and it also has more width. Higher stiffness and strength of the specimen DL is due to better distribution of the force in the infilled panel as well as more compression struts in the distributed loading. Figure 15 shows stiffness degradation due to compression and tensile damage. It is evident that the cracks have been initiated from the compressive corners. As it can be seen, the damage in finite element models is almost the same as the experimental specimens (Fig. 7). The failure modes of the models are in good agreement with the experiment, as well.

### 3.3 Specimen MM

For further controlling of the obtained results and due to the lack of experimental data regarding the investigation of effects of the loading condition on masonry infilled frames, another test setup has been chosen. This infilled frame has the same aspect ratio as the experimental specimens but with a weaker frame. This experimental research conducted by

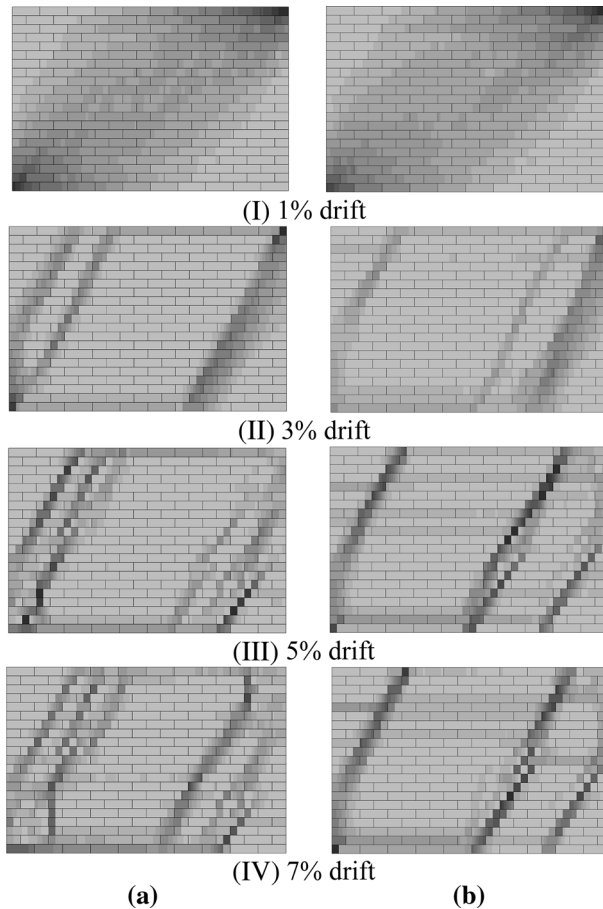


**Fig. 14** Principal compressive stresses in the infill panels of each specimen in different drifts **a** Specimen DL, **b** Specimen CL

Moghadam et al. (2006) merely includes testing of masonry infilled steel frames subjected to concentrated lateral loading. A finite element model of Moghadam et al. (2006) under concentrated loading is developed and validated against the experimental data. Then, distributed lateral loading is applied to this analytical model that eventually led to same conclusions as those of the first finite element model. This indicates that the obtained results from experimental and analytical study do not depend on the test setup arrangement.

Eleven medium and small scaled reinforced and unreinforced specimens were tested under concentrated loading. Among these specimens, the one which is related the most to the current study is picked. This specimen is an unreinforced masonry infilled steel frame and is referred to as specimen MM. The test setup of specimen MM is shown in Fig. 16a.

According to this figure, the infill panel is 220 cm high and 286 cm wide. The infilled frame consists of beams and columns of single IPE140 sections. Plastic moment capacity and modulus of elasticity of 25.3 kN m and 170 GPa, respectively, were obtained through a material test for steel sections. The beam flanges were directly connected to the column

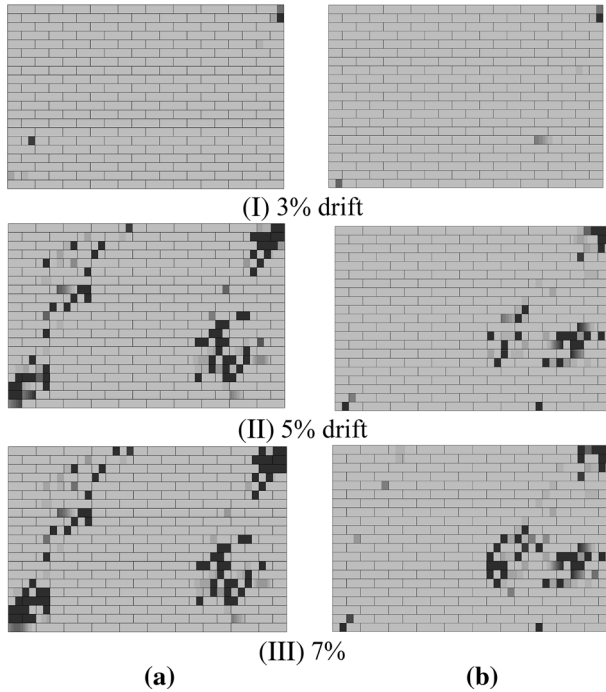


**Fig. 15** Stiffness degradation due to compression and tensile damage in different drifts **a** Specimen DL, **b** Specimen CL

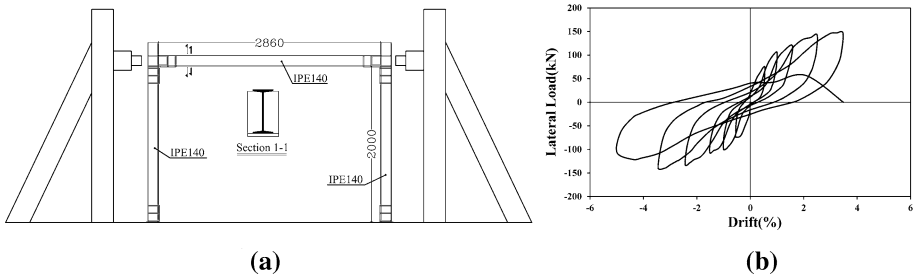


**Fig. 16** **a** Moghadam et al. (2006) test setup (dimensions are in mm), **b** Load-drift curve of Moghadam et al. (2006) specimen

flanges; therefore, the frame connections can be considered rigid.  $300 \times 100 \times 10$  mm bearing plates were placed at each side of the panel zone in order to provide adequate contact surfaces. As shown in Fig. 16a, the concentrated lateral load is applied horizontally by two hydraulic jacks at each side of the infilled frame.

The infill panel thickness in this specimen is 10 cm and made of solid brick units with the dimensions of  $194 \times 98 \times 56$  mm. Material test showed that Prism specimens had modulus of elasticity of 2300 MPa. Also, the values of 3–7 MPa were obtained for compressive strength in material test done on three prism specimens.

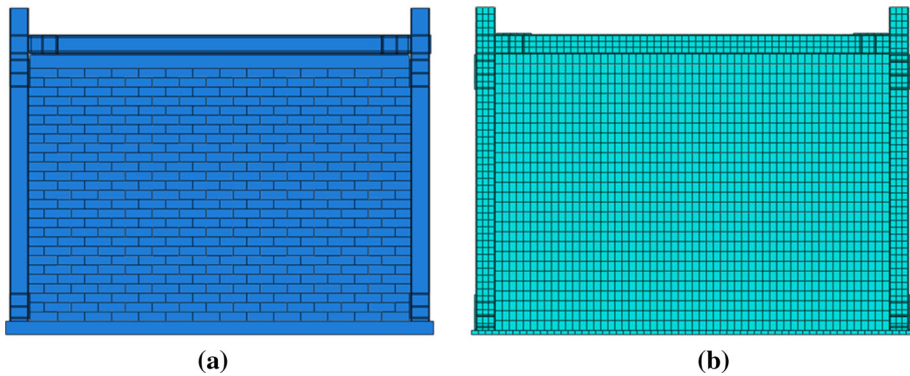


**Fig. 17** Geometry and mesh details of specimen MM (Moghadam et al. 2006) **a** Specimen geometry **b** Mesh details of the specimen

Figure 16b illustrates the lateral load-drift curve of the Moghadam et al. (2006) specimen. The maximum strength of this specimen (150 kN) occurs at the drift of 3.5%.

The finite element model of specimen MM is developed which its geometry and mesh details is indicated in Fig. 17. Table 4 lists the important material properties that are required for modeling.

### 3.3.1 Finite element analysis results

In order to verify monotonic behavior of Moghadam et al. (2006) specimen, the envelope curve of its hysteresis curve should be derived. Figure 18 compares the experimental and finite element lateral load-drift curves of the specimens which are in good agreement. The comparison of failure modes in experimental and finite element model of the specimen MM is indicated in Fig. 19.

Therefore after verifying the analytical model of specimen MM against experimental results, the finite element model is subjected to distributed loading in order to affirm the results obtained from the first experimental study. Figure 20 presents lateral load-drift curves of Moghadam et al. (2006) specimen subjected to the concentrated and distributed loadings. It can be seen that the stiffness and ultimate strength of analytical model subjected to distributed loading are 14% and almost 27.5% higher than those of the model under concentrated loading.

Figure 21 shows the principal compressive stresses in the infill panels at the drift of 3%. It illustrates that the finite element model subjected to distributed loading has more compression struts than that of subjected to the concentrated loading. This fact explains the greater strength of analytical model under distributed loading in comparison with that of the model subjected to the concentrated loading.

## 3.4 Parametric study

This section presents the result of parametric study performed on specimens DL and CL. The parametric study is conducted to investigate the effects of different factors on the behavior of the masonry infilled steel frames under distributed and concentrated lateral loading. These factors include number of spans and aspect ratio of the infilled frame. To study how number of spans influences the stiffness and strength of the infilled frame,

**Table 4** Material properties of Infill panel used for verification of FE model (Moghadam et al. 2006)

Property	Value
Density ( $\rho$ )	1812 kg/m <sup>3</sup>
Young's modulus ( $E$ )	2300 MPa
Poisson's ratio ( $\nu$ )	0.15
Compressive strength ( $f'_c$ )	7 MPa
Tensile strength ( $f'_t$ )	1.5 MPa
Strain corresponding to peak stress ( $\epsilon'_c$ )	0.014
Friction coefficient ( $\mu$ )	0.75
Compressive strength of mortar ( $f_m$ )	7.1 MPa
Peak tensile bond strength ( $t_n^0$ )	0.21 MPa
Peak shear bond strength ( $t_s^0$ )	0.39 MPa
Normal stiffness ( $K_n$ )	168 GPa
Shear stiffness ( $K_s$ )	73 GPa
Mode-I fracture energy ( $G_{IC}$ )	0.012 N/mm
Mode-II fracture energy ( $G_{IIC}$ )	0.036 N/mm

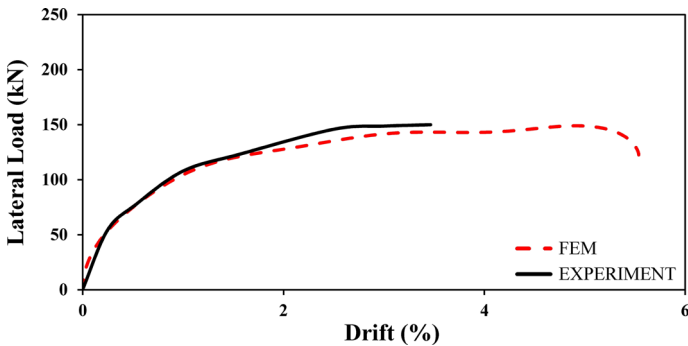


**Fig. 18** The experimental and analytical lateral load-drift curves of specimen MM

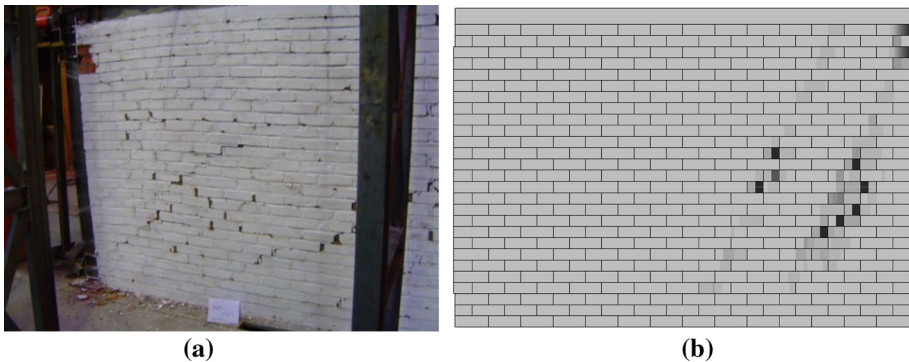


**Fig. 19** Infill crushing in experimental specimen and analytical model **a** Experimental specimen (Moghadam et al. 2006), **b** Finite element model

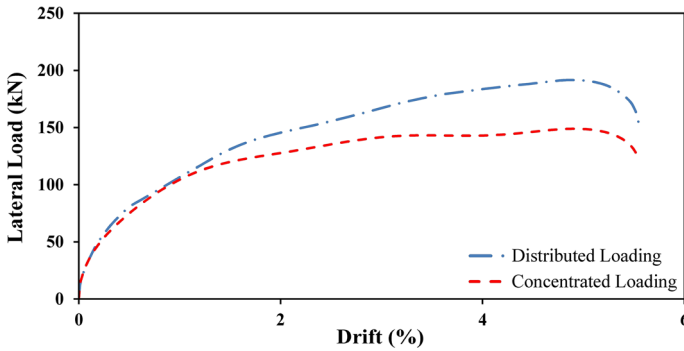


**Fig. 20** Lateral load-drift curves of finite element model subjected to the distributed and concentrated loadings

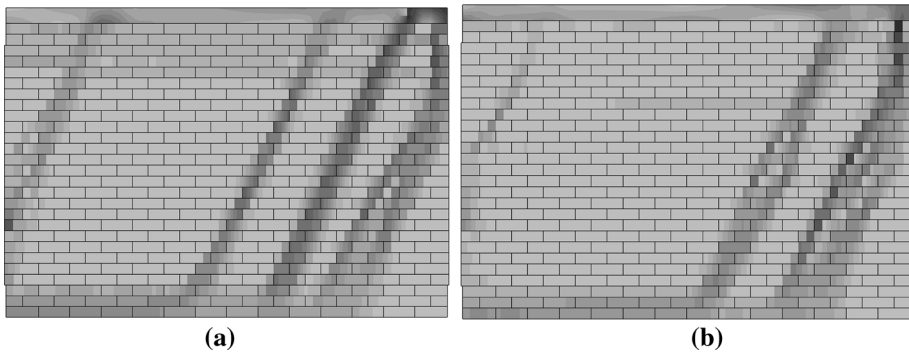


**Fig. 21** Principal compressive stresses in the infill panels at 3% drift **a** Distributed loading, **b** concentrated loading

specimens with 2, 3 and 4 spans are developed and subjected to distributed and concentrated lateral loading. Figure 22a compares lateral load-drift curves of specimens for different number of spans. As it can be seen the difference between the stiffness of infilled frame specimens under distributed and concentrated loading with 2, 3 and 4 number of spans are equal to 28, 26 and 26% respectively. The values that are obtained for ultimate strength in FE analysis are not very precise. Therefore, it is hard to determine a particular

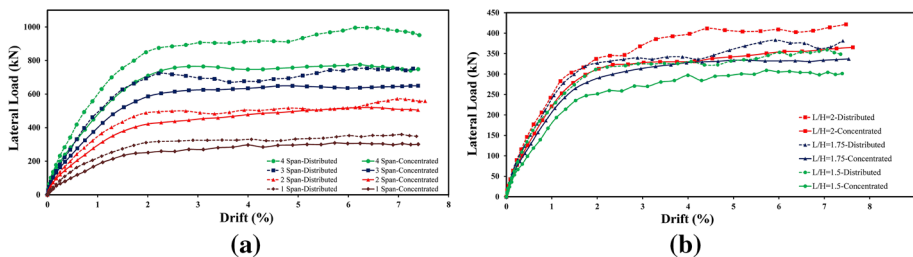


**Fig. 22 a** The effect of number of spans on the lateral load-drift curve of the specimens subjected to distributed and concentrated lateral loading. **b** The effect L/H ratio on the lateral load- drift curve of the specimens subjected to distributed and concentrated lateral loading

difference in ultimate strength of the specimens and this value does not follow a peculiar trend. The minimum and maximum difference in ultimate strength of the infilled frame subjected to distributed and concentrated lateral loading is equal to 10 and 28% for specimens with 2 and 4 spans respectively.

The other important factor in infilled frames is the L/H ratio. The effects of L/H (length to height) ratios of 1.75 and 2 on the strength and stiffness of the masonry infilled frame are studied. Figure 22b compares the lateral load-drift curves of the specimens with different L/H ratios, which includes the L/H ratio of experimental specimens equal to 1.5. It can be seen that bigger L/H ratio results in less difference in stiffness and strength of the infilled frame subjected to distributed and concentrated lateral loading. For instance, the difference in stiffness and strength of the infilled frame with L/H ratio of 2 decreases to 13 and 15% compared to the values mentioned earlier for specimens with L/H ratio of 1.5.

Figures 23 and 24 show infill crushing in infilled frame specimens with 4 spans and L/H ratio of 2, respectively.

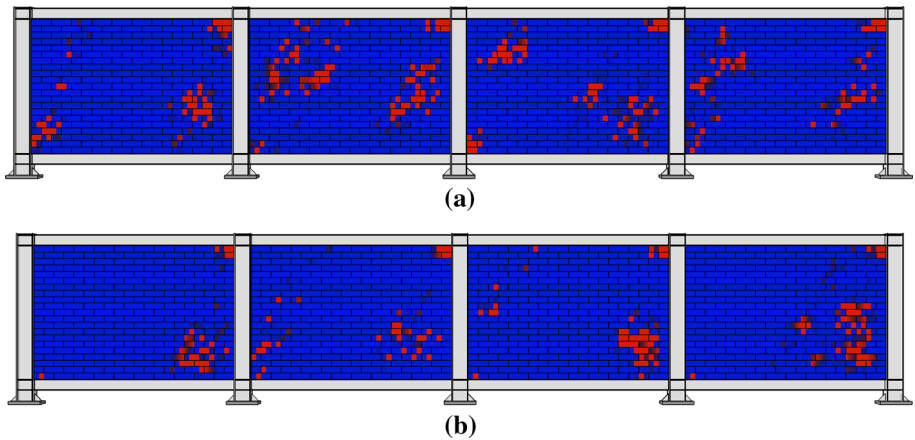


**Fig. 23** Infill crushing in four spans masonry infilled steel frames at 7% drift **a** Distributed loading **b** Concentrated loading

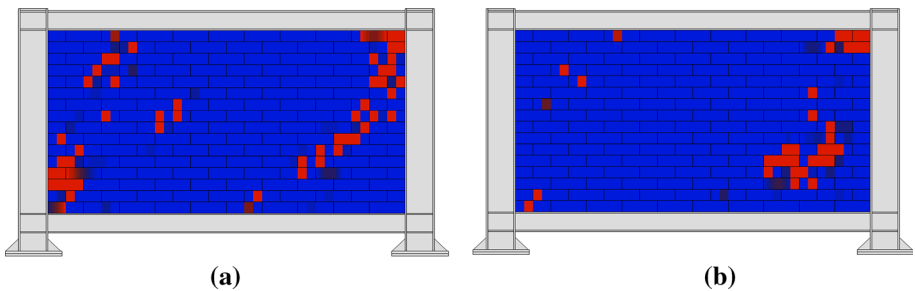


**Fig. 24** Infill crushing in masonry infilled steel frames with L/H ratio of 2 at 7% drift **a** Distributed **b** Concentrated

## 4 Conclusions

This research focused on the effects of different types of lateral loading on the behavior of masonry infilled steel frames. An experimental study is conducted which contains two identical specimens subjected to the distributed and concentrated lateral loadings. The difference in stiffness and strength of the infilled frame specimens under different types of loading is studied using the experimental results. The distribution of force in masonry infilled steel frame is further studied using finite element analysis. Another experimental study is modeled to control that the obtained results do not depend on the test setup arrangement. A parametric study is also performed to investigate how number of spans and aspect ratio of the frame affect the masonry infilled frames behavior.

Following conclusions can be drawn according to the experimental and analytical results:

1. The strength and stiffness of the experimental specimen subjected to the distributed loading is 18.5 and 29% higher than that of the specimen under concentrated loading due to the better distribution of the force in the infilled frame.
2. Experimental study indicates that corner crushing is the predominant failure mode of the specimen CL. However, in specimen DL, corner crushing does not occur at the same drift as specimen CL and although damage can be observed in the corners, corner crushing is not the dominant failure mode. Instead, this specimen has diagonal cracking failure mode, in which two compression struts are created, initiated from the compressive corners.
3. Finite element modeling is able to properly capture the failure modes of the specimens. It also shows the same amount of difference in strength and stiffness of the infilled frame subjected to concentrated and distributed lateral loading.
4. The MM specimen (Moghadam et al. 2006) has different test setup and weaker frame compared to DL and CL specimens. Nevertheless, the finite element investigation on the behavior of this frame under distributed and concentrated lateral loading repeats the same results as the infilled frame specimens experimentally tested in the current study.
5. Based on the parametric study, increasing the number of spans does not result in significant difference between stiffness and strength of the specimen under distributed and concentrated lateral loading. Moreover, investigation on the aspect ratio of the infilled frame indicated that, increasing the value of  $L/H$  ratio might lead to less difference between stiffness and strength.
6. It is illustrated in this study that the formulas of the design codes; such as MSJC (Building Code Requirements for Masonry Structures (MSJC) 2008), which are based on tests with concentrated loading underestimate the stiffness and strength of the masonry infilled steel frames.

**Acknowledgements** This research was financially supported by the International Institute of Earthquake Engineering and Seismology under research No. 7386, which is highly appreciated. The results and conclusions presented in this paper are those of authors and do not necessarily represent point of views and opinions of the sponsor.

## Appendix

See Fig. 25.

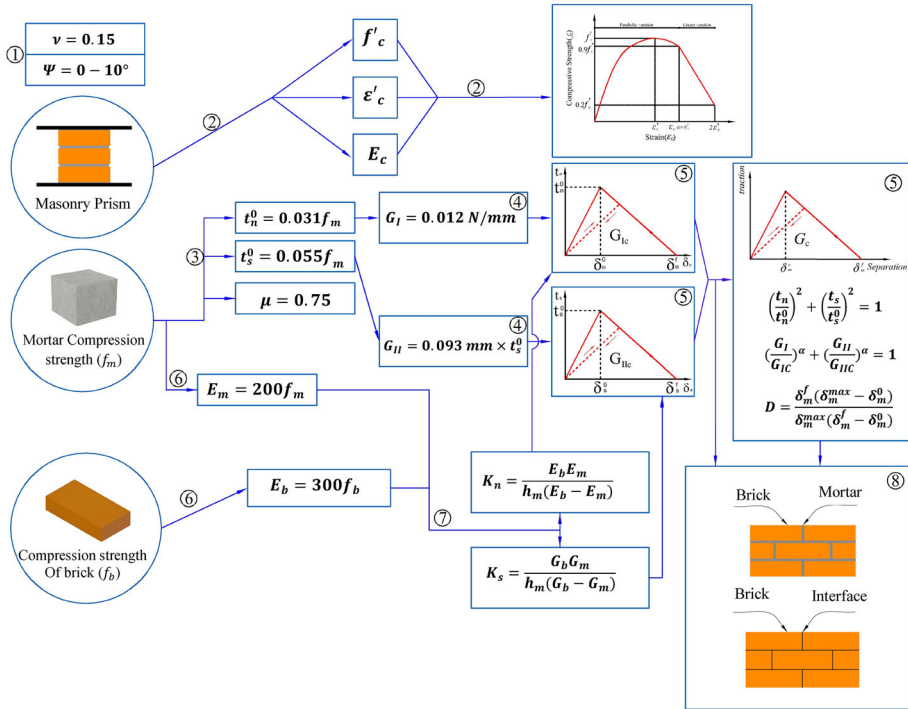


**Fig. 25** Simplified micro modeling procedure. (1) Based on a recommendation by Choudhury et al. (2015) the values of  $10^\circ$  is chosen for the dilation angle. The value of 0.15 is used for Poisson’s ratio (Lourenco 1996). (2) In accordance with a study by Bolhassani et al. (2015) the behavior of prism specimens is determined with material test for using as compressive behavior in FE software. Then the average of parameters including stiffness, maximum strength and its corresponding strain for different specimens is obtained. Using the recommendation by Agnihotri et al. (2013) the Kashik et al. (2007) model was employed to reach a general behavior of the masonry specimens and this behavior was defined in FE software. (3) Using the results of a study by Lumantama et al. (2012), tensile and shear strength of interface are determined as 0.031 and 0.055 of compressive strength of mortar. The friction coefficient was considered equal to 0.75 based on the study by Angelillo et al. (2014). (4) The interface damage starts when the quadratic function equals one (Nazir and Dhanasekar 2013). Using the recommended values by Angelillo et al. (2014)  $G_{IC}$  and the ductility index for shear fracture energy ( $\frac{G_{IIc}}{G_{Ic}^0}$ ) are considered equal to 0.012 N/mm and 0.093 mm. (5) The bilinear curve shows the cohesive behavior and its softening in different conditions (Bolhassani et al. 2015). Power model by Tao (2013) is employed to model decohesion under mixed mode loading. (6) In accordance with results of study by Kaushik et al. (2007)  $E_b$  and  $E_m$  are equal to 300 times compressive strength of brick ( $f_b$ ) and 200 times compressive strength of mortar ( $f_m$ ), respectively. (7) To define the cohesive behavior of the interface normal stiffness ( $K_N$ ) and shear stiffness ( $K_s$ ) should be determined using the formulas by Lourenco et al. (1996). (8) The mortar layer is not modeled and half of the mortar joint thickness is added to the adjacent brick layers. Instead, the cohesive behavior of mortar in three conditions of pure tensile, pure shear and mix mode is assigned to the bricks interface as shown in the chart. As mentioned the friction coefficient is assumed to be 0.75 (Angelillo et al. 2014)

## References

- Agnihotri P, Singhal V, Rai DC (2013) Effect of in-plane damage on out-of-plane strength of unreinforced masonry walls. *Eng Struct* 57:1–11
- Angelillo M, Lourenço PB, Milani G (2014) Masonry behaviour and modelling. In: Angelillo M (ed) *Mechanics of masonry structures*. Springer, pp 1–26
- ASCE/SEI (2007) *Seismic rehabilitation of existing buildings* (ASCE/SEI 41-06)
- Asteris PG, Chrysostomou CZ, Giannopoulos I, Ricci P (2013) Modeling of infilled framed structures. In: Papadrakakis M, Fragiadakis M, Plevris V (eds) *Computational methods in earthquake engineering*. Springer, pp 197–224
- Barua H, Mallick S (1977) Behaviour of mortar infilled steel frames under lateral load. *Build Environ* 12:263–272
- Beyer K, Tondelli M, Petry S, Peloso S (2015) Dynamic testing of a four-storey building with reinforced concrete and unreinforced masonry walls: prediction, test results and data set. *Bull Earthq Eng* 13:3015–3064
- Bolhassani M, Hamid AA, Lau AC, Moon F (2015) Simplified micro modeling of partially grouted masonry assemblages. *Constr Build Mater* 83:159–173
- Building Code Requirements for Masonry Structures (MSJC) (2008). American Concrete Institute, the American Society of Civil Engineers and The Masonry Society, USA
- Caliò I, Marletta M, Pantò B (2012) A new discrete element model for the evaluation of the seismic behaviour of unreinforced masonry buildings. *Eng Struct* 40:327–338
- Camanho PP, Davila C, De Moura M (2003) Numerical simulation of mixed-mode progressive delamination in composite materials. *J Compos Mater* 37:1415–1438
- Choudhury T, Milani G, Kaushik HB (2015) Comprehensive numerical approaches for the design and safety assessment of masonry buildings retrofitted with steel bands in developing countries: the case of India. *Constr Build Mater* 85:227–246
- Chrysostomou C, Gergely P, Abel J (2002) A six-strut model for nonlinear dynamic analysis of steel infilled frames. *Int J Struct Stab Dyn* 2:335–353
- Crisafulli FJ, Carr AJ (2007) Proposed macro-model for the analysis of infilled frame structures. *Bull N Z Soc Earthq Eng* 40:69–77
- Dawe J, Seah C (1989) Behaviour of masonry infilled steel frames. *Can J Civ Eng* 16:865–876
- De Matteis G (2005) Effect of lightweight cladding panels on the seismic performance of moment resisting steel frames. *Eng Struct* 27:1662–1676
- De Matteis G, Landolfo R (1999) Structural behaviour of sandwich panel shear walls: an experimental analysis. *Mater Struct* 32:331–341
- De Matteis G, Landolfo R (2000) Modelling of lightweight sandwich shear diaphragms for dynamic analyses. *J Constr Steel Res* 53:33–61
- Dhanasekar M, Haider W (2008) Explicit finite element analysis of lightly reinforced masonry shear walls. *Comput Struct* 86:15–26
- Dhanasekar M, Page A (1986) The influence of brick masonry infill properties on the behaviour of infilled frames. In: *ICE proceedings*, vol 4. Thomas Telford, pp 593–605
- El-Dakhakhni WW, Elgaaly M, Hamid AA (2003) Three-strut model for concrete masonry-infilled steel frames. *J Struct Eng* 129:177–185
- El-Dakhakhni WW, Hamid AA, Elgaaly M (2004) Seismic retrofit of concrete-masonry-infilled steel frames with glass fiber-reinforced polymer laminates. *J Struct Eng* 130:1343–1352
- FEMA461 (2006) FEMA 461: Interim protocols for determining seismic performance characteristics of structural and nonstructural components through laboratory testing
- Flanagan RD, Bennett RM (1999) In-plane behavior of structural clay tile infilled frames. *J Struct Eng* 125:590–599
- Flanagan RD, Bennett RM (2001) In-plane analysis of masonry infill materials. *Pract Period Struct Des Constr* 6:176–182
- Harper PW, Hallett SR (2008) Cohesive zone length in numerical simulations of composite delamination. *Eng Fract Mech* 75:4774–4792
- Harris HG, Sabnis G (1999) *Structural modeling and experimental techniques*. CRC Press, Boca Raton, FL
- Hibbit H, Karlsson B, Sorensen E (2012) *ABAQUS user manual*, version 6.12. Simulia, Providence
- Holmes M (1961) Steel frames with brickwork and concrete infilling. In: *ICE proceedings*, vol 4. Thomas Telford, pp 473–478
- Ju R-S, Lee H-J, Chen C-C, Tao C-C (2012) Experimental study on separating reinforced concrete infill walls from steel moment frames. *J Constr Steel Res* 71:119–128

- Kaushik HB, Rai DC, Jain SK (2007) Stress-strain characteristics of clay brick masonry under uniaxial compression. *J Mater Civ Eng* 19:728–739
- Klingner RE, Bertero VV (1976) Infilled frames in earthquake-resistant construction, Rep. No. EERC 76-32. University of California, Berkeley, CA
- Krätzig WB, Pölling R (2004) An elasto-plastic damage model for reinforced concrete with minimum number of material parameters. *Comput Struct* 82:1201–1215
- Krstevska L, Tashkov L, Gocevski V, Garevski M (2010) Experimental and analytical investigation of seismic stability of masonry walls at Beauharnois powerhouse. *Bull Earthq Eng* 8:421–450
- Kumar N, Amirtham R, Pandey M (2014) Plasticity based approach for failure modelling of unreinforced masonry. *Eng Struct* 80:40–52
- Liauw T, Kwan K (1983) Plastic theory of non integral infilled frames. In: *ICE Proceedings*, vol 3. Thomas Telford, pp 379–396
- Liauw T, Lee S (1977) On the behaviour and the analysis of multi-storey infilled frames subject to lateral loading. In: *ICE Proceedings*, vol 3. Thomas Telford, pp 641–656
- Liu Y, Manesh P (2013) Concrete masonry infilled steel frames subjected to combined in-plane lateral and axial loading—An experimental study. *Eng Struct* 52:331–339
- Liu Y, Soon S (2012) Experimental study of concrete masonry infills bounded by steel frames. *Can J Civ Eng* 39:180–190
- Lourenco PB (1996) Computational strategies for masonry structures. TU Delft, Delft University of Technology, Delft
- Lourenço PB, Avila L, Vasconcelos G, Alves JPP, Mendes N, Costa AC (2013) Experimental investigation on the seismic performance of masonry buildings using shaking table testing. *Bull Earthq Eng* 11:1157–1190
- Lubliner J, Oliver J, Oller S, Onate E (1989) A plastic-damage model for concrete *International. J Solids Struct* 25:299–326
- Lumantarna R, Biggs DT, Ingham JM (2012) Compressive, flexural bond, and shear bond strengths of in situ New Zealand unreinforced clay brick masonry constructed using lime mortar between the 1880s and 1940s. *J Mater Civ Eng* 26:559–566
- Madan A, Reinhorn A, Mander J, Valles R (1997) Modeling of masonry infill panels for structural analysis. *J Struct Eng* 123:1295–1302
- Mainstone R (1971) On the stiffnesses and strengths of infilled frames. *Proc Inst Civil Eng* iv(7360s):59–70
- Mainstone RJ, Weeks G (1972) The influence of a bounding frame on the racking stiffness and strengths of brick walls. *Building Research Station*
- Mehrabi AB, Shing PB, Schuller MP, Noland JL (1996) Experimental evaluation of masonry-infilled RC frames. *J Struct Eng* 122:228–237
- Minaie E, Moon FL, Hamid AA (2014) Nonlinear finite element modeling of reinforced masonry shear walls for bidirectional loading response. *Finite Elem Anal Des* 84:44–53
- Mochizuki S (1988) Inelastic behavior of framed shear wall governed by slip failure of wall panel. *Ratio* 1:2–7
- Moghadam H, Mohammadi MG, Ghaemian M (2006) Experimental and analytical investigation into crack strength determination of infilled steel frames. *J Constr Steel Res* 62:1341–1352
- Moghaddam H (2004) Lateral load behavior of masonry infilled steel frames with repair and retrofit. *J Struct Eng* 130:56–63
- Mohammadi M, Akrami V, Mohammadi-Ghazi R (2010) Methods to improve infilled frame ductility. *J Struct Eng* 137:646–653
- Mohammed A-G (2006) Experimental comparison of brickwork behaviour at prototype and model scales. Dissertation, Cardiff University
- Mohammed A, Hughes T (2011) Prototype and model masonry behaviour under different loading conditions. *Mater Struct* 44:53–65
- Mohebbi S, Mirghaderi SR, Farahbod F, Sabbagh AB, Torabian S (2016) Experiments on seismic behaviour of steel sheathed cold-formed steel shear walls clad by gypsum and fiber cement boards. *Thin-Walled Struct* 104:238–247
- Mohyeddin A, Goldsworthy HM, Gad EF (2013) FE modelling of RC frames with masonry infill panels under in-plane and out-of-plane loading. *Eng Struct* 51:73–87
- Moradabadi E, Laefer DF, Clarke JA, Lourenço PB (2015) A semi-random field finite element method to predict the maximum eccentric compressive load for masonry prisms. *Constr Build Mater* 77:489–500
- Nazir S, Dhanasekar M (2013) Modelling the failure of thin layered mortar joints in masonry. *Eng Struct* 49:615–627
- Page A (1981) The biaxial compressive strength of brick masonry. In: *ICE proceedings*, vol 3. Thomas Telford, pp 893–906

- Pereira JM, Campos J, Lourenço PB (2015) Masonry infill walls under blast loading using confined underwater blast wave generators (WBWG). *Eng Struct* 92:69–83
- Petry S, Beyer K (2014) Scaling unreinforced masonry for reduced-scale seismic testing. *Bull Earthq Eng* 12:2557–2581
- Pluijm R (1999) Out-of-plane bending of masonry behaviour and strength. Technische Universiteit Eindhoven
- Polliakov SVe (1963) Masonry in framed buildings: An investigation into the strength and stiffness of masonry infilling. National Lending Library for Science and Technology
- Pölling R (2000) Eine praxisnahe, schädigungsorientierte Materialbeschreibung von Stahlbeton für Strukturanalysen. Ruhr-Universität Bochum. Dissertation, (in German)
- Saneinejad A, Hobbs B (1995) Inelastic design of infilled frames. *J Struct Eng* 121:634–650
- Sathiparan N, Anjalee W, Kandage K (2016) The scale effect on small-scale modelling of cement block masonry. *Mater Struct* 49:2935–2946
- Smith BS, Carter C A (1969) Method of analysis for infilled frames. In: ICE Proceedings, vol 1. Thomas Telford, pp 31–48
- Smith BS, Coull A (1991) Tall building structures: analysis and design. Wiley, New York
- Tao Y (2013) Fibre reinforced polymer (FRP) strengthened masonry arch structures. Dissertation, The University of Edinburgh
- Thiruvengadam V (1985) On the natural frequencies of infilled frames. *Earthq Eng Struct Dyn* 13:401–419
- Tiberti S, Acito M, Milani G (2016) Comprehensive FE numerical insight into Finale Emilia Castle behavior under 2012 Emilia Romagna seismic sequence: damage causes and seismic vulnerability mitigation hypothesis. *Eng Struct* 117:397–421
- Tomažević M, Weiss P (2010) Displacement capacity of masonry buildings as a basis for the assessment of behavior factor: an experimental study. *Bull Earthq Eng* 8:1267–1294
- UBC (1997) Uniform Building Code 97, Code for seismic design of buildings (1997 Edition) vol 2
- Wood R (1978) Plasticity, composite action and collapse design of unreinforced shear wall panels in frames. In: ICE Proceedings, vol 2. Thomas Telford, pp 381–411
- Wu SR, Gu L (2012) Introduction to the explicit finite element method for nonlinear transient dynamics. Wiley, Hoboken, New Jersey